Journal of Applied Physics

The equation of state of $TaC_{0.99}$ by X-ray diffraction in radial scattering geometry to 32 GPa and 1073 K

Cite as: J. Appl. Phys. **126**, 105107 (2019); https://doi.org/10.1063/1.5115350
Submitted: 17 June 2019 . Accepted: 16 August 2019 . Published Online: 10 September 2019

S. Speziale, J. Immoor, A. Ermakov, S. Merkel, H. Marquardt, and H.-P. Liermann

Journal of Applied Physics ARTICLE scitation.org/journal/jap

The equation of state of $TaC_{0.99}$ by X-ray diffraction in radial scattering geometry to 32 GPa and 1073 K

Cite as: J. Appl. Phys. **126**, 105107 (2019); doi: 10.1063/1.5115350
Submitted: 17 June 2019 · Accepted: 16 August 2019 ·
Published Online: 10 September 2019

S. Speziale,[1,a)] J. Immoor,[2] A. Ermakov,[3] S. Merkel,[4] H. Marquardt,[2,5] and H.-P. Liermann[3]

AFFILIATIONS

[1]German Research Centre for Geosciences GFZ, Telegrafenberg, D-14473 Potsdam, Germany
[2]Bayerisches Geoinstitut (BGI), University of Bayreuth, 95440 Bayreuth, Germany
[3]Photon Sciences, Deutsches Elektronen Synchrotron (DESY), FS-PETRA-D, 22607 Hamburg, Germany
[4]Univ. Lille, CNRS, INRA, ENSCL, UMR 8207 - UMET - Unité Matériaux et Transformations, F-59000 Lille, France
[5]Department of Earth Sciences, University of Oxford, South Parks Road, Oxford OX1 3AN, United Kingdom

[a)]**Author to whom correspondence should be addressed:** speziale@gfz-potsdam.de

ABSTRACT

We have performed *in situ* synchrotron X-ray diffraction experiments on $TaC_{0.99}$ compressed in a diamond anvil cell along 3 isothermal paths to maximum pressure (P)-temperature (T) conditions of 38.8 GPa at 1073 K. By combining measurements performed in axial diffraction geometry at 296 K and in radial geometry at 673 K and 1073 K, we place constraints on the pressure-volume-temperature (P-V-T) equation of state of TaC in a wide range of conditions. A fit of the Birch-Murnaghan equation to the measurements performed in axial geometry at ambient temperature yields a value of the isothermal bulk modulus at ambient conditions $K_{T0} = 305 \pm 5\,(1\sigma)$ GPa and its pressure derivative $(\partial K_T/\partial P)_{T0} = 6.1 \pm 0.5$. The fit of the Birch-Murnaghan-Debye model to our complete P-V-T dataset allows us to constrain the Grüneisen parameter at ambient pressure $\gamma_0 = V(\partial P/\partial E)_{V0}$ to the value of 1.2 ± 0.1.

I. INTRODUCTION

Tantalum carbide, TaC_x $(0.6 < x < 1)$, is a B1 structured ultrahigh-temperature ceramic (UHTC).[1] UHTC materials have the potential to be used in different technological applications because of their combined high mechanical strength, extremely good thermal stability, as well as their resistance to harsh chemical environments.

Transition metal carbides (TMCs) are in general among the ceramic materials with the best characteristics for high-temperature applications where enhanced refractory and mechanical properties are required.[2] Tantalum carbide has an extremely high melting temperature, low electrical conductivity, and unusual mechanical behavior with respect to the other B1 structured (space group $Fm\bar{3}m$) monocarbides of the group IV and V transition metals.[3,4]

The structural, thermodynamic, and transport properties of TaC_x (in the following, we will use TaC except when discussing the effect of nonstoichiometry on specific physical properties) have been the subject of many experimental and computational investigations, and part of the existing results are tabulated in several review publications together with the properties of other TMCs.[5–27] In particular, the elastic properties of TaC have been the subject of more than ten different experimental and computational studies[6,15,16,28–39] exploring the effect of pressure or temperature and nonstoichiometry on the tensor and the aggregate elastic moduli of single crystals or polycrystals.

While several computational studies provide models of the isothermal compression behavior of TaC, only two experimental diamond anvil cell studies investigate its compression behavior to the multi-GPa stress range at ambient temperature.[32,37] The first study focuses on the response of micrometer-sized polycrystalline $TaC_{0.98}$ to compression under different stress conditions, and the second explores the behavior of nanocrystalline TaC under strongly nonhydrostatic stress.

To date, there are no data on the combined effect of high-pressure, stress, and temperature on the structure and thermoelastic properties of tantalum carbide. With this study, we give a first account of the compression behavior of $TaC_{0.99}$ compressed to more than 40 GPa at ambient temperature and to a maximum of 38.8 GPa at 1073 K, and we place quantitative constraints on the pressure-volume-temperature (PVT) equation of state of this material.

Here, we use a new approach to place quantitative constraints on the thermoelastic properties of $TaC_{0.99}$. We combine the results of static compression experiments in a graphite resistive heated diamond anvil cell using *in situ* synchrotron X-ray diffraction in radial scattering geometry (an established technique[40–46] yet never used before in studies dedicated to constrain the pressure-volume-temperature equation of state) with those from axial geometry at room temperature. The use of high-temperature high-pressure radial diffraction geometry in combination with a theory of nonhydrostatic lattice strains allows us to quantitatively constrain the departure from hydrostatic stress conditions, which is not straightforward in experiments performed in axial geometry. This is particularly relevant for stiff samples such as TaC when they bridge between the culets of the two diamond anvils under combined high pressure and high temperature. In addition, the experimental approach used here allows us to measure high-temperature volume compression along strictly isothermal compression paths at moderately high temperatures, which is difficult with laser-heated diamond anvil cell experiments, thus producing the best suited dataset for the *P-V-T* equation of state fitting.

II. MATERIALS AND METHODS

A. Sample material

The starting material for all experiments presented here is a powder of $TaC_{0.99}$ (with nominal stoichiometric TaC composition) produced by American Elements©. We have determined the chemical composition of our starting material by measuring its unit-cell volume by X-ray diffraction at the German Research Centre for Geosciences (GFZ) using a STOE Stadi P diffractometer with Cu K_α radiation monochromatized by a Ge(111) crystal. Two separate amounts of the sample were mixed with ∼10 wt. % Si standard (NIST 640d) as an internal calibrant. The average of the two measurements yields a unit-cell parameter $a_0 = 4.4555 \pm 0.0007$ Å. This value corresponds to a composition of $TaC_{0.99}$ based on the calibration by Bowman.[8] The unit-cell parameter of our sample is equivalent within uncertainty to the results of neutron diffraction measurements of a disordered stoichiometric TaC[9] and 3σ larger (rather than smaller, as expected) than a more recent neutron diffraction study of nominally stoichiometric TaC.[10]

B. High-pressure synchrotron X-ray diffraction in axial geometry

In these experiments, the axis of the diamond anvils is parallel to the incident X-ray beam.

$TaC_{0.99}$ was compressed quasihydrostatically in a symmetric piston-cylinder type diamond anvil cell[47] with 300 μm culet diamonds. Fine sample powder (with less than 1 μm average grain size) was loaded in a 150 μm wide cylindrical chamber drilled in a 250 μm thick rhenium disk preindented to a thickness of 30 μm. Neon gas was loaded as a pressure transmitting medium using the gas-loading facility from Core Labs located at PETRA III and operated by the Extreme Condition Science Infrastructure. A ruby sphere and a ∼5 μm speckle of gently packed gold powder were used as internal pressure standards.[48,49] The diamond anvil cell was compressed remotely with a gas membrane system. X-ray diffraction images were collected at the general purpose experimental table of the Extreme Conditions Beamline (ECB, P02.2) of the 3rd generation light source PETRA III at DESY, Hamburg, Germany. The monochromatic incident X-ray radiation had a wavelength of 0.2966 Å. The beam was focused to a spot size of 3 μm (vertical) by 8 μm (horizontal) full width at half maximum by means of compound refractive lenses (CRL). X-ray diffraction images were collected with a Perkin Elmer XRD1621 flat panel detector at 420 mm distance from the sample. The sample to detector distance and tilting angles of the detector were calibrated using a CeO_2 standard from the National Institute of Standards and Technology (NIST, 674b). Twenty X-ray diffraction images were collected at pressures between 5.1 GPa and 43.6 GPa, including 3 images collected during decompression. The exposure time for each image was 20 s. The images were analyzed with the Fit2d software package.[50] Le Bail fit[51] of the integrated spectra were performed with the software MAUD[52] to determine the unit-cell parameter *a* (TaC crystallizes in the cubic system in the space group $Fm\bar{3}m$). A typical X-ray diffraction image and the result of the Le Bail fit are shown in Fig. 1. The conditions and the results of the room temperature compression experiments are reported in Tables I and II.

C. Simultaneous high-pressure high-temperature synchrotron X-ray diffraction in radial scattering geometry

Two series of measurements were performed in radial scattering geometry at the general purpose experimental table of the ECB. In these experiments, the axis of the diamond anvils is perpendicular to the incident X-ray beam, passing through an X-ray transparent sample chamber, made of a mixture of amorphous boron and epoxy.

The setup for these experiments is based on a modified Mao-Bell piston-cylinder type diamond anvil cell equipped with a graphite resistive sandwich heater for high-temperature experiments.[53] Pressure in the diamond anvil cell is controlled remotely by a gas membrane system. For temperature measurements, two type-R thermocouples are placed in contact with the diamond at short distance from the culets. The diamond anvil cell is placed in a vacuum vessel (capable of maintaining 10^{-4} mbar pressure during the experiments) to protect the diamonds, the metallic parts of the diamond anvil cell, and the heater setup from oxidation.[54]

$TaC_{0.99}$ powder with a grain size <1 μm was loaded in 50 μm diameter cylindrical chambers laser-drilled in amorphous boron–epoxy gaskets of 380 μm diameter and 50 μm thickness. With such a narrow sample chamber, the entire sample remains as close as possible to the center of the diamond culets, where stress gradients are low and where stress and strain fields are close to ideal axial symmetry that is required in the interpretation of X-ray diffraction experiments in radial scattering geometry (see Sec. II D). The ceramic gaskets are supported by a Kapton ring. In all the experiments, the diameter of the diamond culets was 300 μm and no pressure transmitting medium was employed.

In the two high-temperature experimental runs, a 5–10 μm wide fragment of less than 5 μm thick Au foil was placed above the sample as a pressure calibrant. The two high-temperature experimental runs were performed using a monochromatic X-ray beam

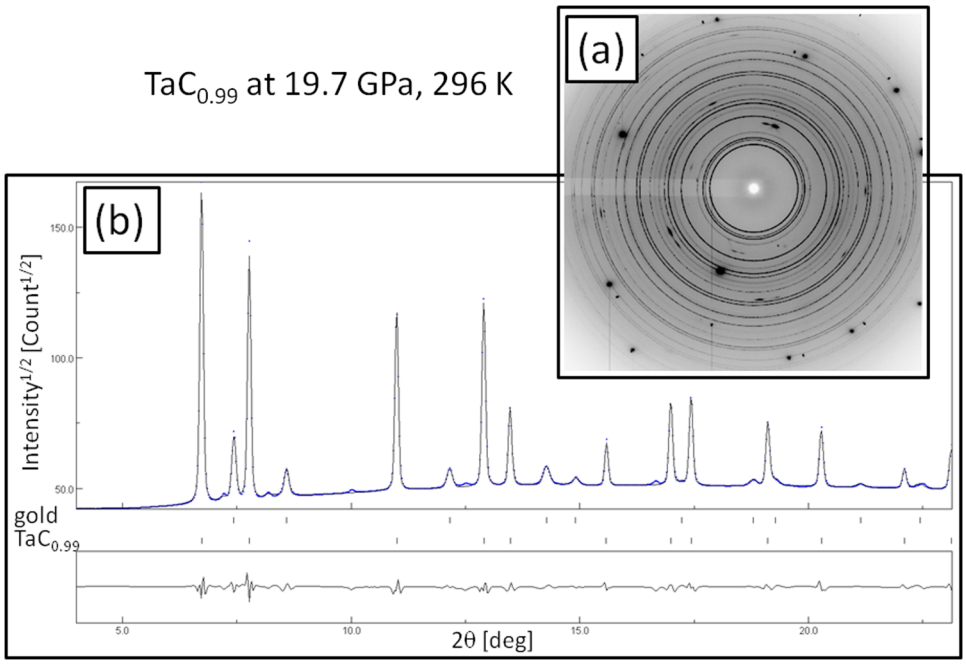

FIG. 1. X-ray diffraction of $TaC_{0.99}$ compressed in an Ne pressure transmitting medium to 19.7 GPa at ambient temperature. (a) X-ray diffraction image; (b) Integrated pattern and LeBail calculated best-fit spectrum. The bars underneath the pattern are the calculated positions of the diffraction peaks of TaC and of gold (used as an internal pressure standard). The misfit is also plotted as the difference between calculated and observed amplitudes.

of 0.4847 Å wavelength with an identical focus spot size as for the axial diffraction experiment but a slightly different sample to detector distance of 405 mm based on the same calibration approach as for the axial diffraction experiment.

The exposure time for all images in the radial X-ray diffraction experiments was 4 s. The images were processed using Fit2d.[50] Each image was integrated in 5° azimuthal (ψ) sectors, for a total of 72 patterns per image. The sets of patterns were further analyzed with the MAUD software package to determine unit cell parameter and nonhydrostatic stress contribution[55] (see Sec. II D).

TABLE I. Experimental condition of the four X-ray diffraction datasets. "Cold compr." is the maximum sample pressure before starting heating.

Experiment	TaC-Ne	TaC-HT1	TaC-HT2
Diffraction geometry	Axial	Radial	Radial
X-ray wavelength (Å)	0.2966	0.4847	0.4847
DAC type	Symmetric P-C	Modif. Mao-Bell	Modif. Mao-Bell
Diamond anvil culet (μm)	300	300	300
P transmitting medium	Ne	No	No
P calibrant	Au, ruby	Au	Au
Temperature (K)	296	673	1073
N data points	20	22	25
Max *P* (GPa)	43.6	33.6	38.8
Exp time (s)	20	4	4
Max membrane *P* (bar)	28.4	58.9	65.0
Exp duration (h)	3	5	6
Cold compr. (GPa)		2.4	2.6

In ideal conditions, the geometry of the diamond anvil cell imposes a cylindrical symmetry of stress and strain at the center of the sample chamber (i.e., along the culets' axial direction). The stress state far from the center of the culets is more complex.[56] For this reason, at each pressure step, the optimized position was determined by X-ray absorption scans along the vertical and horizontal direction. An additional diffraction image of gold was collected at each compression step for pressure calibration at high temperatures.[49]

In both the 673 K and 1073 K runs, the sample was compressed at ambient temperature to 2.5 ± 1 GPa and then progressively heated to the target temperature at an average rate of 3.2 °C/min and 4.6 °C/min, respectively. A total of 47 X-ray diffraction images were collected along two isotherms at 673 K and 1073 K. The parameters of all the experimental runs are reported in Table I.

D. Data analysis of radial diffraction data with MAUD

All radial X-ray diffraction images were analyzed using the MAUD software package. MAUD determines both crystal structure parameters and texture by combining Rietveld full-spectrum fitting and a selection of models to describe crystallite sizes, microstrains, macroscopic stress, and the crystals' preferred orientation.[53,57]

In radial X-ray diffraction experiments, the sample is subject to strongly nonhydrostatic macroscopic stress because it is loaded without any soft pressure transmitting medium. The X-ray diffraction images display anisotropic strains caused by the uniaxial stress applied to the sample. This results in noncircular Debye diffraction rings, with their ellipticity being related to the amount of deviatoric stress and the elastic moduli of the sample material. Specialized theories to describe nonhydrostatic crystal strains have been

TABLE II. Summary of the all the experimental results from all the three runs. "stdev *P* + *V*-TaC" is the complete uncertainty on pressure including the propagation of the uncertainty on the unit-cell volume of $TaC_{0.99}$. "<*Q*>" is the isotropic aggregate value of *Q*, a measure of the strain due to the deviatoric component of the stress applied to the sample (see main text). "*PV* fit" indicates whether the data points were used or not in the isothermal (296 K) *P*-*V* equation of state fit. "PVT fit" indicates whether the data points were used or not in the *P*-*V*-*T* equation of state fit.

Experiment	*T* (K)	*P* (GPa)	*V* (Å^3)	stdev *P* + *V* TaC (GPa)	<*Q*>	*PV* fit	*PVT* fit
TaC-Ne	296	5.1 ± 0.1	87.06 ± 0.01	0.19	…	Yes	Yes
TaC-Ne	296	6.4 ± 0.2	86.71 ± 0.02	0.31	…	Yes	Yes
TaC-Ne	296	10.3 ± 0.1	85.79 ± 0.02	0.22	…	Yes	Yes
TaC-Ne	296	11.6 ± 0.1	85.47 ± 0.02	0.20	…	Yes	Yes
TaC-Ne	296	14.5 ± 0.3	84.81 ± 0.02	0.35	…	Yes	Yes
TaC-Ne	296	17.3 ± 0.5	84.21 ± 0.04	0.67	…	Yes	Yes
TaC-Ne	296	19.7 ± 0.6	83.82 ± 0.04	0.82	…	Yes	Yes
TaC-Ne	296	22.2 ± 0.6	83.35 ± 0.04	0.84	…	Yes	Yes
TaC-Ne	296	24.6 ± 0.5	82.91 ± 0.04	0.74	…	Yes	Yes
TaC-Ne	296	27.1 ± 0.4	82.43 ± 0.04	0.66	…	Yes	Yes
TaC-Ne	296	29.5 ± 0.5	82.02 ± 0.04	0.76	…	Yes	Yes
TaC-Ne	296	31.6 ± 0.5	81.64 ± 0.01	0.60	…	Yes	Yes
TaC-Ne	296	34.1 ± 0.6	81.21 ± 0.01	0.64	…	Yes	Yes
TaC-Ne	296	36.4 ± 0.8	80.83 ± 0.01	0.82	…	Yes	Yes
TaC-Ne	296	38.4 ± 0.6	80.48 ± 0.01	0.66	…	Yes	Yes
TaC-Ne	296	40.8 ± 0.8	80.07 ± 0.01	0.81	…	Yes	Yes
TaC-Ne	296	43.6 ± 0.7	79.63 ± 0.01	0.77	…	Yes	Yes
TaC-Ne	296	38.9 ± 0.8	80.47 ± 0.01	0.83	…	No	Yes
TaC-Ne	296	32.0 ± 0.7	81.72 ± 0.02	0.68	…	No	Yes
TaC-Ne	296	18.8 ± 1.0	84.11 ± 0.04	1.06	…	No	Yes
TaC-Ne	296	0.0001	88.478 ± 0.003	0.001	…	Yes	Yes
TaC-HT1	673 ± 20	7.4 ± 0.3	86.95 ± 0.10	0.68	0.0009	No	Yes
TaC-HT1	674 ± 20	6.0 ± 0.3	87.10 ± 0.11	0.70	0.0010	No	No
TaC-HT1	673 ± 20	6.8 ± 0.3	86.89 ± 0.09	0.64	0.0011	No	No
TaC-HT1	673 ± 20	8.2 ± 0.3	86.68 ± 0.09	0.66	0.0012	No	No
TaC-HT1	673 ± 20	9.4 ± 0.3	86.46 ± 0.11	0.75	0.0014	No	Yes
TaC-HT1	682 ± 20	11.0 ± 0.3	86.17 ± 0.10	0.72	0.0015	No	Yes
TaC-HT1	673 ± 20	12.6 ± 0.3	85.71 ± 0.11	0.78	0.0018	No	Yes
TaC-HT1	673 ± 20	15.3 ± 0.4	85.13 ± 0.10	0.81	0.0022	No	Yes
TaC-HT1	673 ± 20	17.4 ± 0.4	84.61 ± 0.11	0.89	0.0024	No	Yes
TaC-HT1	671 ± 20	20.0 ± 0.4	83.99 ± 0.10	0.89	0.0030	No	Yes
TaC-HT1	667 ± 20	23.6 ± 0.4	83.39 ± 0.11	0.97	0.0035	No	Yes
TaC-HT1	672 ± 20	26.5 ± 0.4	82.84 ± 0.10	0.99	0.0040	No	Yes
TaC-HT1	672 ± 20	28.4 ± 0.5	82.42 ± 0.11	1.07	0.0041	No	Yes
TaC-HT1	673 ± 20	30.7 ± 0.5	81.96 ± 0.10	1.04	0.0044	No	Yes
TaC-HT1	673 ± 20	32.2 ± 0.5	81.52 ± 0.10	1.10	0.0046	No	Yes
TaC-HT1	673 ± 20	33.0 ± 0.5	81.51 ± 0.09	1.05	0.0047	No	Yes
TaC-HT1	672 ± 20	33.6 ± 0.5	81.54 ± 0.11	1.16	0.0042	No	Yes
TaC-HT1	674 ± 20	24.6 ± 0.4	83.09 ± 0.11	1.00	0.0014	No	Yes
TaC-HT2	297	1.9 ± 0.3	87.98 ± 0.05	0.43	0.0006	No	Yes
TaC-HT2	297	1.8 ± 0.3	87.98 ± 0.05	0.44	0.0005	No	Yes
TaC-HT2	297	2.6 ± 0.3	87.80 ± 0.06	0.49	0.0007	No	Yes
TaC-HT2	1073 ± 60	2.9 ± 0.2	88.57 ± 0.13	0.67	0.0012	No	Yes
TaC-HT2	1072 ± 60	3.0 ± 0.2	88.47 ± 0.12	0.63	0.0017	No	Yes
TaC-HT2	1074 ± 60	3.0 ± 0.2	88.46 ± 0.12	0.64	0.0016	No	Yes
TaC-HT2	1073 ± 60	2.9 ± 0.2	88.54 ± 0.12	0.65	0.0013	No	Yes
TaC-HT2	1069 ± 60	2.9 ± 0.2	88.54 ± 0.13	0.65	0.0014	No	Yes
TaC-HT2	1071 ± 60	2.8 ± 0.2	88.58 ± 0.12	0.61	0.0015	No	Yes
TaC-HT2	1072 ± 60	2.9 ± 0.2	88.66 ± 0.12	0.64	0.0015	No	Yes
TaC-HT2	1073 ± 60	3.0 ± 0.2	88.66 ± 0.13	0.68	0.0016	No	Yes

TABLE II. (*Continued.*)

Experiment	T (K)	P (GPa)	V (Å^3)	stdev $P+V$ TaC (GPa)	<Q>	PV fit	PVT fit
TaC-HT2	1073 ± 60	3.1 ± 0.2	88.68 ± 0.13	0.66	0.0014	No	Yes
TaC-HT2	1072 ± 60	3.2 ± 0.2	88.66 ± 0.11	0.61	0.0015	No	Yes
TaC-HT2	1056 ± 60	3.2 ± 0.2	88.59 ± 0.12	0.63	0.0018	No	Yes
TaC-HT2	1075 ± 60	3.7 ± 0.2	88.48 ± 0.12	0.65	0.0020	No	Yes
TaC-HT2	1074 ± 60	11.3 ± 0.3	86.29 ± 0.11	0.75	0.0027	No	Yes
TaC-HT2	1075 ± 60	11.4 ± 0.3	86.23 ± 0.11	0.76	0.0029	No	Yes
TaC-HT2	1073 ± 60	12.0 ± 0.3	86.08 ± 0.13	0.85	0.0030	No	Yes
TaC-HT2	1074 ± 60	13.4 ± 0.3	85.77 ± 0.13	0.88	0.0033	No	Yes
TaC-HT2	1073 ± 60	14.7 ± 0.3	85.49 ± 0.12	0.85	0.0036	No	Yes
TaC-HT2	1073 ± 60	17.9 ± 0.4	84.75 ± 0.12	0.92	0.0039	No	Yes
TaC-HT2	1072 ± 60	20.7 ± 0.4	84.20 ± 0.13	0.99	0.0040	No	Yes
TaC-HT2	1073 ± 60	23.3 ± 0.4	83.73 ± 0.14	1.07	0.0041	No	Yes
TaC-HT2	1074 ± 60	25.4 ± 0.4	83.35 ± 0.12	1.01	0.0042	No	Yes
TaC-HT2	1072 ± 60	27.5 ± 0.4	82.95 ± 0.14	1.15	0.0042	No	Yes
TaC-HT2	1073 ± 60	29.4 ± 0.4	82.65 ± 0.12	1.12	0.0043	No	Yes
TaC-HT2	1075 ± 60	31.5 ± 0.5	82.38 ± 0.12	1.15	0.0043	No	Yes
TaC-HT2	1074 ± 60	32.9 ± 0.5	82.04 ± 0.12	1.14	0.0044	No	No
TaC-HT2	1073 ± 60	34.9 ± 0.5	81.78 ± 0.12	1.21	0.0046	No	No
TaC-HT2	1073 ± 60	36.1 ± 0.5	81.52 ± 0.13	1.29	0.0046	No	No
TaC-HT2	1072 ± 60	37.8 ± 0.5	81.28 ± 0.12	1.25	0.0048	No	No
TaC-HT2	1073 ± 60	38.8 ± 0.5	81.09 ± 0.14	1.37	0.0049	No	No

developed to analyze the X-ray diffraction images collected from samples compressed in the diamond anvil cell and other high-pressure devices.[57–59] In our analysis, here, we are interested in the study of the (volume) compression of TaC, and we correct for the effect of nonhydrostaticity by using the theory developed by Singh.[58] Here, we assume that the $TaC_{0.99}$ polycrystalline aggregate sample behaves as an elastically isotropic material. Following the formulation presented by Singh[58] for the isotropic aggregate case,

$$d_d(hkl) = d_p(hkl)[1 + (1 - 3\cos^2\psi)Q], \quad (1)$$

where $d_d(hkl)$ is the d-spacing of the (hkl) lattice planes family as determined in the pattern integrated at an angle ψ measured anti-clockwise from the compression direction. $d_p(hkl)$ is the d-spacing under hydrostatic stress (corresponding to pressure P) and Q is a measure of the strain due to the deviatoric component of the stress. For isotropic aggregates of elastically anisotropic materials and assuming that stress is homogeneous in the aggregate, Singh[58] derives

$$\langle Q\rangle = t(1+\nu)/3E = t/6G, \quad (2)$$

where $\langle Q\rangle$ is the isotropic aggregate Q, averaged on all the diffracting lattice families [see Eq. (1)], $t = \sigma_3 - \sigma_1$ is the difference between the normal stress along the compression axis and perpendicular to it, ν is average Poisson's ratio, E is Young's modulus of the isotropic aggregate sample, and G is the isotropic aggregate shear modulus. The model of Singh[58] is incomplete for aggregates subject to plastic deformation and with large density of defects.[60] However, Eq. (1) has been shown to be useful to describe such experimental data, extract average stress levels,[45] and model the plastic behavior of materials using more advanced methods.[61]

The unit-cell parameter a corresponding to the hydrostatic stress component is determined from the spectrum at $\psi = 54.7°$. The implementation of the model available in MAUD allowed us to fix the values of ν and E and refine the values of σ_3 and σ_1 to fit the observed d-spacings. We calculated the value of $\langle Q\rangle$ using Eq. (2). This can finally be easily converted [see Eq. (1)] into the nonhydrostatic stress contribution to the uncertainty on the unit-cell parameter. The uncertainties due to nonhydrostatic conditions are in average of the order of 10^{-2} Å, substantially larger than the estimated uncertainties on the values of the unit-cell parameter refined with the full-spectrum fit, which are of the order of 10^{-4} Å.

A typical X-ray diffraction image collected in radial scattering geometry is shown in Fig. 2(a). The unrolled sequence of patterns integrated at 5° azimuthal-angle steps (see Sec. II) is presented in Fig. 2(b) together with the fit result.

In both the experiments performed at 673 K and 1073 K, pressure was determined by fitting the unit-cell parameter of gold, loaded together with the sample in the sample chamber. The analysis of X-ray diffraction of gold was performed similarly to that of the sample material itself. The stress/lattice strain analysis generally gave results of deviatoric stress comparable with those of the $TaC_{0.99}$ sample. In some cases, the fit of stress and lattice strain of gold did not converge to consistent results due to the lower than average gold diffraction signal.

The 3 X-ray diffraction images collected at 6.0, 6.8, and 8.2 GPa at 673 K and the 5 ones collected at 1073 K from 32.9 to 38.8 GPa show a deviation from the ideal geometry, with a maximum of

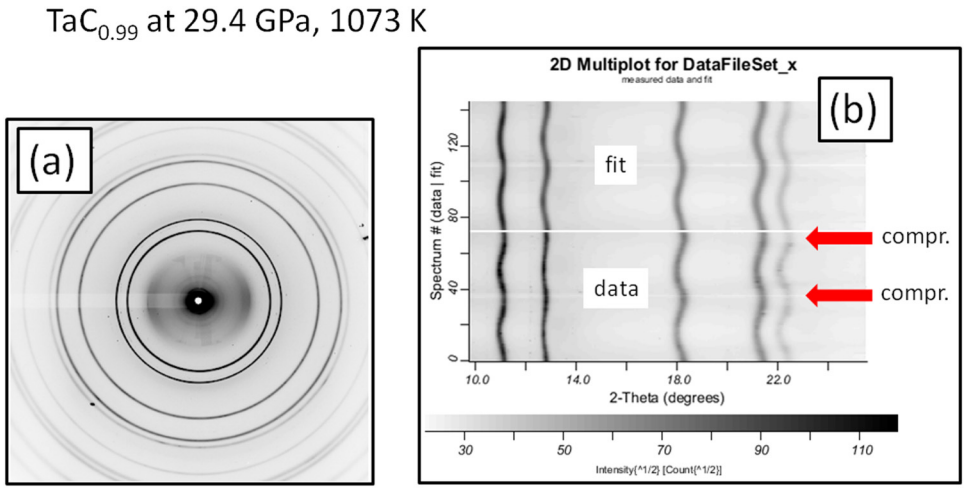

FIG. 2. Radial X-ray diffraction of $TaC_{0.99}$ compressed without pressure transmitting medium to 29.4 GPa at 1073 K. (a) X-ray diffraction image; (b) Sequence of patterns integrated from 5° azimuthal sectors and the fit model calculated by MAUD software (the arrows indicate the compression direction parallel to the diamond anvils axes).

lattice strains in a direction tilted with respect to the diamond anvil axis (Fig. 3). Nonideal stress conditions are typically due to gasket partial failure at the highest pressures (as in the case of the 1073 K isotherm) or, less frequently, at the lowest pressures, at the first contact between the diamond culets and the ceramic gasket (as in the case of the 673 K isotherm). Nevertheless, we also performed a full analysis of these images and we will discuss the results below.

All parameters determined by Rietveld analysis of the diffraction images of $TaC_{0.99}$ in the two radial X-ray diffraction experimental runs are reported in Table II.

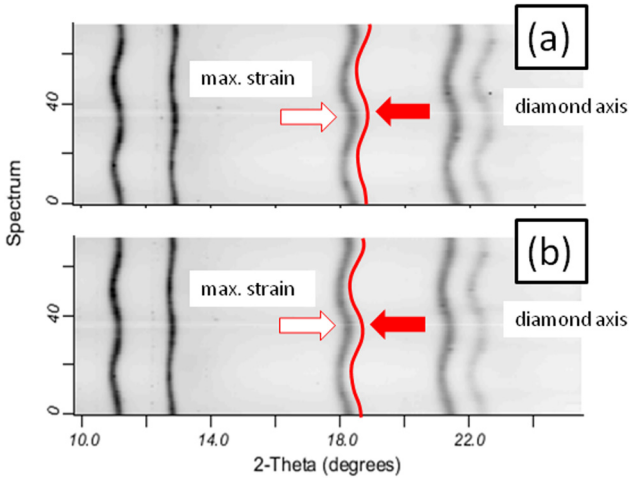

FIG. 3. Example of radial X-ray diffraction measurement in nonideal sample geometry. (a) Sequence of azimuthally integrated patterns from the radial X-ray diffraction image collected at 38.8 GPa and 1073 K. The direction of the diamond axes (red arrow) does not correspond to that of maximum strain of the sample (white arrow). (b) Ideal case (29.4 GPa and 1073 K): the direction of maximum strain corresponds to the diamond axis direction.

E. *P-V-T* equation of state analysis

A third order Birch-Murnaghan *P-V* equation of state[62] was fitted to the unit-cell volumes of $TaC_{0.99}$ measured in the experiment performed in axial geometry and quasihydrostatic stress at ambient temperature. Pressures were determined from the unit-cell volume of gold loaded in the diamond anvil cell together with the sample.[49] The pressure-volume data were weighted by the pressure uncertainties on the measurements of both gold and $TaC_{0.99}$ propagated from the uncertainties of their respective experimentally determined unit-cell volumes.

The three coefficients of the third order Birch-Murnaghan equation are the unit-cell volume at ambient conditions V_0, the isothermal bulk modulus at ambient conditions K_{T0}, and its isothermal pressure derivative at ambient conditions $(\partial K_T/\partial P)_{T0}$. We fixed the value of V_0 to the one we measured at the GFZ (see above), and we refined the values of K_{T0} and $(\partial K_T/\partial P)_{T0}$. The individual data points used in the fit are reported in Table III ("TaC-Ne"). In the fit, we did not consider all the data points collected in decompression; however, we will mention, in the Discussion, their effect on the fit results. After the first decompression step, the piston and cylinder of the diamond anvil cell were jammed. We observed a sudden decrease of sample (and Au standard) unit-cell volume between each of the decompression points. The decompression volume–pressure data do not plot on the

TABLE III. Best-fit parameters of the *P-V-T* equation of state of $TaC_{0.99}$ based on our experimental data.

This study	Parameter	1σ stdev
V_0 (Å^3)	88.478	0.020
K_{T0} (GPa)	305	5
$(dK_T/dP)_{T0}$	6.1	0.5
γ_{th0}	1.2	0.1
q	1	2
θ_0 (K)	567	10

compression dataset, even though they overlap within reciprocal pressure uncertainties. Our interpretation is that, due to the sudden stress release, the stress field applied to the sample was different with respect to that generated by the smooth stress increase in compression, and the anomalous stress condition affected the pressure determination. The last data point, collected at 1 bar after complete pressure release, overlaps with the ambient conditions X-ray diffraction measurement and refinements performed at the GFZ (see Fig. 4).

The pressure-volume data of $TaC_{0.99}$ collected in radial diffraction geometry along the two high-temperature isotherms at 673 K and 1073 K were used to fit the parameters of the Birch-Murnaghan-Debye *P-V-T* equation of state (e.g., Ref. 63). Pressures were determined from the measured unit-cell volume of gold loaded in the diamond anvil cell together with the sample. Error propagation of the uncertainties on the sample and gold experimental unit-cell volumes was performed using the same strategy as for the room temperature quasihydrostatic experimental dataset. We additionally weighted the data of the high-temperature runs (performed without soft pressure transmitting medium) by propagating the additional volume strain caused by the uniaxial stress present in the sample chamber (see Sec. II D). The uncertainty on temperature in the experimental setup used in this study is estimated to be ±20 K at 673 K and ±60 K at 1073 K.[53]

The coefficients of the Birch-Murnaghan-Debye equation are V_0, K_{T0}, and $(\partial K_T/\partial P)_{T0}$ for the reference isotherm, which we fixed to be the ambient temperature isotherm. Three thermal parameters were refined: the Grüneisen parameter at ambient conditions γ_0, its logarithmic volume derivative $q = (\partial \ln \gamma/\partial \ln V)_T$, and the Debye temperature at ambient conditions θ_0. Due to our limited dataset, we fixed the initial unit-cell volume of the reference isotherm (V_0) to our own measurement result and the value of θ_0 to 567 ± 10 K, which is the average of the available literature data[19,24,30,31,36,39] excluding the two extreme values.[34,37] We thus refined the values of q and γ_0, for which the extant published results are in strong disagreement with each other.[17,31,36]

The whole dataset used to fit the parameters of the equation of state of $TaC_{0.99}$ are reported in Table II.

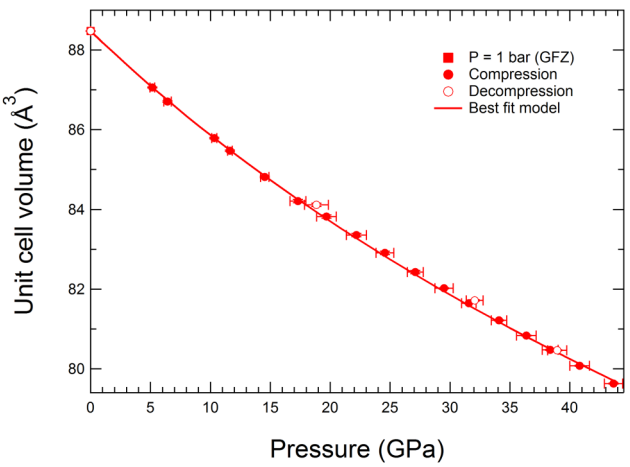

FIG. 4. Isothermal compression of $TaC_{0.99}$ at ambient temperature (296 K). The dataset used for the analysis is that of experiment TaC-Ne (see text). The data collected in decompression were not used for the fit of the *P-V* equation of state.

III. RESULTS

A. Isothermal equation of state of $TaC_{0.99}$ at 296 K

The unit-cell volumes determined in the quasihydrostatic experiment are reported in Table II. The compression curve is plotted in Fig. 4. The third order Birch-Murnaghan fit of our data yields $K_{0T} = 305 \pm 5$ GPa and $(\partial K_T/\partial P)_{T0} = 6.1 \pm 0.5$, where K_{0T} is the initial bulk modulus and $(\partial K_T/\partial P)_{T0}$ is its initial pressure derivative. We performed our fit by fixing V_0 (the initial unit-cell volume) to the value of 88.478 Å^3 based on our measurement at ambient pressure. The root mean square (RMS) misfit of the pressure dataset is 0.29 GPa. We tested the effect of including the three decompression data points (those collected at 38.9, 32.0, and 18.8 GPa) in the fitted dataset. The fitted coefficients are insensitive, within estimated uncertainties, to the inclusion of the decompression data. However, the RMS misfit increases by more than 20% by adding these three data points, and we decided to exclude them in our final fit (see Table II). The model isothermal compression curve is plotted as a solid line in Fig. 4.

B. *P-V-T* equation of state of $TaC_{0.99}$

The high-temperature unit-cell volumes dataset (Table II) combined with the parameters of the ambient temperature isotherm were used to fit the thermal coefficients of a Birch-Murnaghan-Debye equation of state. We did not include in the dataset the data collected at 6.0, 6.8, and 8.2 GPa at 673 K and the 5 ones collected at 1073 K from 32.9 to 38.8 GPa (see also Sec. IV). In the fit, we fixed the value of θ_0 to 570 ± 10 K averaged between the available literature data (see Sec. II). The fit yields an initial value of the Grüneisen parameter $\gamma_0 = 1.2 \pm 0.1$. The value of the logarithmic pressure derivative of the Grüneisen parameter (q) is poorly constrained by the current dataset and the best-fit value is $q = 1 \pm 2$. The RMS pressure misfit of the full high-temperature dataset is equal to 0.46 GPa. The complete set of coefficient of the pressure-volume-temperature equation of state of $TaC_{0.99}$ based on our experimental results is reported in Table III. The experimental unit-cell volumes and the model isotherms at 296 K, 673 K, and 1073 K are plotted in Fig. 5.

IV. DISCUSSION

A. Isothermal equation of state of $TaC_{0.99}$ at 296 K

The values of $K_{0T} = 305 \pm 5$ and $(\partial K_T/\partial P)_{T0} = 6.1 \pm 0.5$ constrained by our new quasihydrostatic dataset compare well with the available computational and experimental results for TaC_x (Table IV).

Several *ab initio* density functional theory (DFT) computational studies have investigated the elastic properties of TaC using either local density approximation (LDA), generalized gradient approximation (GGA), Perdew-Burke-Ernzerhof (PBE), revised Perdew-Burke-Ernzerhof (RPBE) functional, or Perdew-Wang functional (PW91)

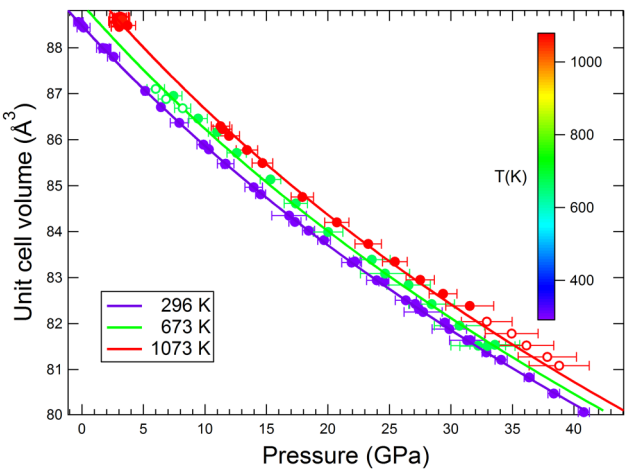

FIG. 5. *P-V-T* compression behavior of $TaC_{0.99}$. The data used for fitting are colored as a function of the experimental temperature following the color scale displayed in the legend. The curves are the best-fit model *P-V* isotherms at the temperatures of the 3 datasets (296 K, 673 K, and 1073 K). The white-filled symbols correspond to data points in nonideal geometry (see text), which were not used for the fit.

for the exchange-correlation electronic interaction.[6,13,15,18,33–39] The values of the ambient pressure bulk modulus are generally similar in all the studies when the same approximation is used for the exchange-correlation electronic interaction. The average for the studies using GGA is 315 ± 16 GPa and overlaps with our result within reciprocal 1σ uncertainties. One of the computational studies[33] combines DFT calculations and experimental ultrasonic interferometry data, for only two of the three elastic stiffness coefficients of TaC. Using the elastic anisotropy expressed as the Zener anisotropy ratio $A = 2C_{44}/(C_{11} - C_{12})$,[64] from their calculations, we can estimate the value of the experimental bulk modulus $K_{0S} = 310$ GPa, which agrees with our result within 1σ. Here, we point out that the difference between the isothermal bulk modulus K_{0T} and the isentropic bulk modulus K_{0S} expressed by the thermodynamic relationship $K_{0S} = K_{0T}(1 + \alpha\gamma T)$ (where α is the thermal expansion coefficient and γ is the Grüneisen parameter) in the case of TaC is of the order of 3 ± 1 GPa, which is comparable with the uncertainties of all the existing experimental studies (Table IV).

Our best-fit K_{0T} is at the lower end of the values of isothermal and isentropic bulk modulus reported in the literature except for a single-crystal ultrasonics study of $TaC_{0.90}$[29] and a neutron inelastic scattering study of single-crystal TaC[17] which yield $K_{0S} = 217 \pm 12$ GPa and $K_{0S} = 283$ GPa, respectively. The three studies performed on $TaC_{0.99}$ present values of the isentropic bulk modulus K_{0S} between 345 GPa and 317 GPa,[28,30,65] all calculated by extrapolation to full density of ultrasonic experimental studies of porous ceramic materials. If we consider all the available data from elasticity studies including a study of $TaC_{0.98}$,[31] the average value of 335 ± 13 GPa is compatible with our fitted value only at 3σ uncertainty level.

Only three experimental and three computational studies investigated the pressure dependence of the elastic moduli of TaC_x.[16,31–33,36,37] The pressure derivatives $(\partial K_T/\partial P)_{T0}$ based on experimental studies[31,32,37] are equal to 4.97 ± 0.27, 4.0 ± 0.4, and 4, respectively, and are substantially different from our result. However, the pressure derivative presented in Ref. 31 is calculated from ultrasonic pulse-echo measurements of a compressed porous sample without direct measurements of the sample volume. The value reported in Ref. 37 is based on a high-pressure X-ray diffraction study of nanoparticle TaC, which could have a different elastic behavior with respect to the bulk material (see, for instance, the case of MgO[66]) and it has been fixed in the data analysis. The results of Ref. 32 are based on a similar approach as the one used in the present study, and the large disagreement deserves a more detailed explanation. Liermann *et al.*[32] performed high-pressure X-ray powder diffraction of $TaC_{0.98}$ compressed in the diamond anvil cell using Al as a pressure transmitting medium. Even though Al is a metal with low shear modulus at ambient conditions, it represents a strong pressure medium if compared to Ne at pressures of tens of gigapascals. The use of strong pressure transmitting media unavoidably produces deviatoric stress in the sample chamber. In axial X-ray diffraction geometry, the crystallites that contribute to the measured signal are those with diffracting vectors (the directions normal to the diffracting lattice planes) close to perpendicular to the diamond axes, and thus subject to deviatoric extension (relative to the ideal hydrostatic strain).[58] This causes underestimation of volume compression and overestimation of the material bulk modulus.[66,67] In addition to this, the value of bulk modulus and pressure derivative at ambient conditions obtained by fitting high-pressure X-ray diffraction results suffer from trade-offs between the two coefficients of the fitted equation of state.[68] In order to better compare the results of the two studies, we have plotted the difference between the *P-V* isotherms calculated using the two sets of parameters and a common starting volume (Fig. 6). This procedure corresponds to comparing pressures along the two isotherms at the same values of compression. The difference between the two compression curves is within three times the average uncertainty of our data if we include the error propagated from the unit-cell volume uncertainty. If we consider that the experimental uncertainties on pressure and unit-cell volume in Ref. 32 are of the same order of magnitude as the one in our dataset, the disagreement between the two isothermal equations of state is within 2σ reciprocal uncertainties. The similarity between the compression curves of $TaC_{0.99}$ and $TaC_{0.98}$ suggests that, within experimental uncertainties, the isothermal compressibility of TaC_x at 300 K is only marginally sensitive to low levels of nonstoichiometry ($0.98 \leq x < 1$).

The pressure derivative of the bulk modulus from the four *ab initio* computational studies with local density approximation (LDA),[33] generalized gradient approximation (GGA),[36] and with both approximations[16,37] is in all cases substantially smaller (between 29% and 42%) than our result. However, this is partially compensated by their larger bulk modulus at room pressure. The discrepancy between our experimental results and *ab initio* computations could be due to the presence, in our sample material, of a complex defect structure in addition to slight nonstoichiometry, which includes dislocations, grain boundaries, and microstrains associated with them. Indeed, it has been observed that carbon-defective TaC_x ceramics show higher mechanical strength than stoichiometric TaC.[3] The characterization of defect states and their

TABLE IV. Comparison of our best-fit thermoelastic parameters for $TaC_{0.99}$ and all the available literature data. "PTM" is the pressure transmitting medium. "*E*" is the isotropic aggregate Young's modulus. "Poisson's" is the isotropic aggregate Poisson's ratio. All the parameters refer to ambient conditions.

Reference	Method	Composition	V_0 (Å^3)	Density (g/cm^3)	K_0 (GPa)	G (GPa)	$(dK/dP)_0$	E (GPa)	Poisson's
This study	A-XRD + R-XRD	$TaC_{0.99}$	88.478	14.448	305 ± 5		6.1 ± 0.5		
Brown *et al.* (1966)[28]	Thin rod Ultrasound resonance	$TaC_{0.994}$	88.424	14.489	344	216		537	0.24
Bartlett and Smith (1967)[29]	Ultrasound pulse-echo	$TaC_{0.90}$		14.65	217 ± 7	120 ± 25		304 ± 64	0.27
Jun and Shaffer (1971)[30]	Ultrasound resonance	$TaC_{0.99}$	88.359	14.496	345	216.8		537.7	
Smith and Gläser (1970)[17]	Neutron Inelastic Scattering	TaC	88.448	14.491	283[a]	194		474	0.22
Bukatov *et al.* (1975)[65]	Ultrasound pulse-echo	$TaC_{0.99}$			317	227		552	0.21
Dodd *et al.* (2003)[31]	Ultrasound pulse-echo	$TaC_{0.98}$		14.478	332 ± 39	234 ± 27	4.97 ± 0.25	567 ± 68	0.215
Liermann *et al.* (2005)[32]	A-XRD (Al PTM)	$TaC_{0.98}$			340 ± 5		4[b]		
	A-XRD (nonhydrostatic)	$TaC_{0.98}$			347 ± 2		4[b]		
	A-XRD (all data)	$TaC_{0.98}$			345 ± 9		4 ± 0.4		
López de-la-Torre *et al.* (2005)[33]	Ultrasound resonance	TaC		14.64					
	DFT (LDA)	TaC	85.533	14.985	365 ± 4		3.6 ± 0.2		
	DFT (GGA)	TaC	92.652	13.833	318 ± 4	191		550	0.21
Wu *et al.* (2005)[34]	DFT (LDA)	TaC	85.184	15.046	357	215		536	0.25
Shanoun *et al.* (2005)[16]	DFT (LDA)	TaC	84.605	15.149	397.6	390	3.64	882	0.13
	DFT (GGA)	TaC	89.915	14.254	318.98	313	4.34	708	0.13
Isaev *et al.* (2007)[13]	DFT (GGA)	TaC	89.315	14.350	324				
Lu *et al.* (2007)[35]	DFT (GGA) + Debye-Grüneisen	TaC			317	162		514	0.23
Peng *et al.* (2009)[36]	DFT (GGA)	TaC	94.756	13.526	311	188	4.32	470	0.248
Li *et al.* (2011)[15]	DFT (LDA)	TaC	86.586	14.802	365.3	168.8		438.8	0.3
	DFT (GGA-PBE)	TaC	95.069	13.482	304.9	120.9		320.3	0.32
	DFT (RPBE)	TaC	95.194	13.464	303.1	120.6		319.5	0.32
	DFT (PW91)	TaC	95.256	13.455	302.3	117.6		312.3	0.33
Chen *et al.* (2013)[37]	A-XRD	TaC nano	88.478	14.486	433 ± 7		4[b]		
	DFT (LDA)	TaC	88.478	14.486	371 ± 3	274	4.29	660	0.21
	DFT (GGA)	TaC	88.478	14.486	310 ± 2	221	4.25	537	0.21
Liu *et al.* (2014)[38]	DFT (GGA)	TaC	96.072	13.341	293.5	166.4		491.8	0.221
Sai Gautam and Hari Kumar (2014)[39]	DFT (GGA-PBE)	TaC	87.884	14.584	344	229		563	0.227
Yu *et al.* (2014)[6]	DFT (GGA)	TaC	89.315	14.350	340	214		531	0.24

[a]The elastic coefficients are not presented in the original paper.
[b]Parameter fixed in the analysis of the data.

energetics in TaC has been subject of several computational and theoretical studies.[69,70] A recent study has shown that increasing C vacancies concentration reduces the elastic moduli of TaC_x.[71] However, it is not yet clear what effect this deficiency has on the pressure dependence of bulk modulus. The isothermal compression curves of all the existing high-pressure studies of TaC_x[16,31–33,36,37] are calculated with the same procedure as of Ref. 32 (see above) and compared with ours in Fig. 6.

B. *P-V-T* equation of state of $TaC_{0.99}$

Our full high-pressure/high-temperature dataset places a strong constrain on the value of $\gamma_0 = 1.2 \pm 0.1$. In the framework

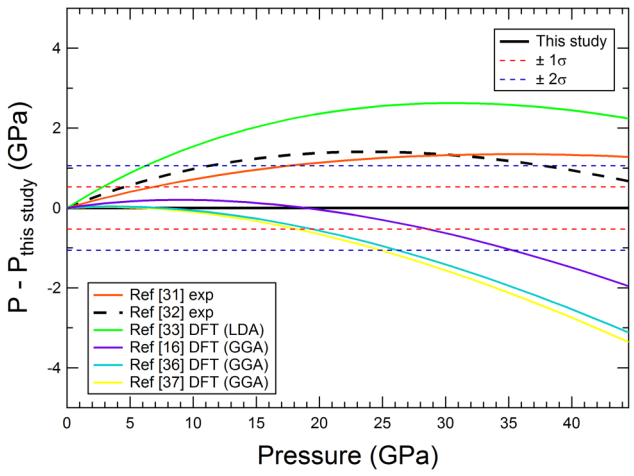

FIG. 6. Comparison of the 296 K *P-V* equation of state of $TaC_{0.99}$ with the other available models for TaC_x compositions. The disagreement is expressed as the difference between the pressures calculated for the different models and our equation of state at the same values of Eulerian strain. The differences are plotted vs the pressure calculated with our equation of state (in abscissas). In the legend, "exp" indicates experimental studies and "DFT" indicates computational studies using the density functional theory.

of the Birch-Murnaghan-Debye model, this coefficient is the thermodynamic Grüneisen parameter at ambient conditions. This value is obtained by fitting both our full dataset, or after removing the 3 data points at 6.0, 6.8, and 8.2 GPa at 673 K and the 5 data for 32.9, 34.9 36.1, 37.9, and 38.8 GPa at 1073 K due to their nonideal geometry (see Sec. II). Our best-fit value of γ_0 compares very well with the value of the elastic Grüneisen parameter $\gamma_{el} = 1.222$ determined for polycrystalline $TaC_{0.98}$ by ultrasonic techniques.[31] However, the elastic Grüneisen parameter is the average value of the volume dependence of the acoustic phonon frequencies at the Brillouin zone center, a parameter which is different from the thermodynamic Grüneisen parameter $\gamma_{th} = \alpha K_S/(\rho C_p)$ (where α is the volume thermal expansion coefficient, K_S is the isentropic bulk modulus, ρ is density, and C_p is the specific heat at constant pressure), which controls the thermal pressure contribution in the *P-V-T* equation of state. The value of the thermodynamic Grüneisen parameter at ambient conditions calculated from the published thermoelastic properties of TaC_x (Table V) ranges between 1.47 and 2.34, that is 30%–90% larger than the best-fit value to our experimental dataset. The reason for this difference is clearly due to the limitations of the Birch-Murnaghan-Debye model to describe the thermal energy contribution in $TaC_{0.99}$. The high-temperature study of the elastic properties of $TaC_{0.99}$ by Jun and Shaffer[30] shows that the thermodynamic Grüneisen parameter has very strong temperature dependence below 600 K at ambient pressure with a decrease from 1.48 at 300 K to 1.2 at 600 K, and then it remains almost constant at the value of 1.2 at temperatures as high as 1500 K. On the opposite, Peng *et al.*[36] who use the Debye model and a quasiharmonic approximation obtain γ slowly increasing with temperature at ambient pressure (Fig. 7).

The quasiharmonic approximation underlying our equation of state assumes that γ is not explicitly temperature dependent (it is indeed temperature dependent through its volume dependence). This approximation seems to hold for $TaC_{0.99}$ at temperatures above 600 K. The result of the fit to our 673 K and 1073 K isotherms constrains an effective high-temperature value of the ambient pressure thermal Grüneisen parameter, which is more consistent with the results of high-temperature ultrasonic measurements[30] rather than room temperature ultrasonics[30,31] or computations.[36]

The value of q, the logarithmic volume derivative of the Grüneisen parameter, is poorly constrained by our high-temperature dataset. The best-fit value of q is strongly affected by the highest pressure data along the 1073 K isotherm. The fit to our full dataset yields $q = -0.3 \pm 1.4$, while excluding the nonideal data points at 32.9, 34.9 36.1, 37.9, and 38.8 GPa at 1073 K from the fit yields $q = 1 \pm 2$ (see also Sec. III). The average RMS misfit of the full dataset (50 data points) is 0.46 GPa, that of the nonideal 5 data points is 0.59 GPa, while that of all the others is 0.44 GPa. The nonideal data points have a 34% higher disagreement with the fit than all the rest of the dataset. We interpret this as a systematic bias probably connected to the nonideal geometry in these measurements,

TABLE V. Summary of the available results about the thermal properties of TaC_x from the literature.

Reference	Method	Composition	Density (g/cm^3)	α_0 (10^{-6} K^{-1})	C_P (J K^{-1} mol^{-1})	θ_0 (K)	γ_{th}	V_0 (Å^3)
Houska (1964)[20]	EXP	$TaC_{1.02}$	14.538	18				88.270
Kempter (1969)[19]	EXP	$TaC_{0.994}$				572		
Kelley (1940)[21]	EXP	TaC			36.66			
Elliott and Kempter (1958)[22]	EXP	$TaC_{0.984}$	14.491	19.77				88.360
Jun and Shaffer (1971)[23]	EXP	$TaC_{0.99}$		20.01				
Jun and Shaffer (1971)[30]	EXP	$TaC_{0.99}$	14.496			556	1.47	88.360
Dodd *et al.* (2003)[31]	EXP	$TaC_{0.98}$	14.478			593 ± 71		
Lu *et al.* (2007)[35]	COMP	TaC				808	2.34	
Peng *et al.* (2009)[36]	COMP	TaC	13.526	21		541	2.08	94.760
Liu *et al.* (2014)[38]	COMP	TaC	13.341			509.4		96.07
Sai Gautam and Hari Kumar (2014)[39]	COMP	TaC	14.584		38.93	588.3		87.883
Frisk and Fernández Guillermet (1996)[24]	COMP	TaC			36.61	551		

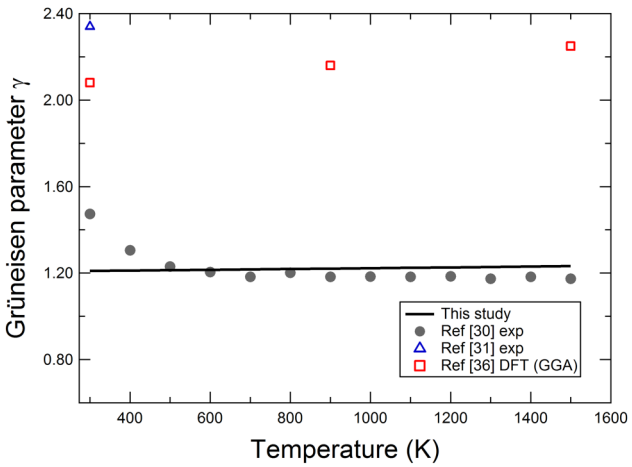

FIG. 7. Temperature dependence of $TaC_{0.99}$ thermodynamic Grüneisen parameter at ambient temperature. The results from our *P-V-T* are compared with the other available results from experimental and computational studies.

and we consider the result of the analysis of the reduced dataset as our best-fit result. The fit results are instead unaffected by including or excluding the 3 nonideal data points at 6.0, 6.8, and 8.2 GPa along the 673 K isotherm. Based on the overall fit of the model isotherms at 673 K and 1073 K, a value of q close to unity is a good approximation of the logarithmic volume sensitivity of γ in the high-temperature regime ($T > 600$ K). This corresponds to

$$\gamma(V) \cong \gamma_0^{HT}(V/V_0), \tag{4}$$

where γ_0^{HT} is the high-temperature, ambient pressure value of $\gamma = 1.2 \pm 0.1$ based on our fit (see discussion above), V represents volume, and V_0 represents the volume at ambient conditions.

In conclusion, our *P-V-T* model is able to successfully describe the pressure-volume-temperature relationship for $TaC_{0.99}$ at 296 K and in the high-temperature range between 673 and 1073 K at pressures as high as 32 GPa, while we expect that it fails to describe the high-pressure behavior of $TaC_{0.99}$ in the ~300–600 K temperature regime, especially at low pressures. The parameters for the high-temperature equation of state of $TaC_{0.99}$ are reported in Table III. The extant published results for TaC_x are reported for comparison in Tables IV and V.

V. CONCLUSIONS

Our extensive experimental investigation gives new information about the compression behavior of $TaC_{0.99}$ under very high pressures and temperatures in the diamond anvil cell. We have constrained the parameters of the *P-V-T* equation of state of $TaC_{0.99}$ to 1073 K and 32 GPa. The ambient pressure derivative of the bulk modulus is substantially higher (50%) with respect to previous studies of the same composition. The thermodynamic Grüneisen parameter refined from our results is lower than the available data at ambient conditions, and it seems to be consistent with the experimental high-temperature limit. The approach used here of determining isothermal equation of state (EOS) data from X-ray diffraction data collected in the radial diffraction geometry under nonhydrostatic conditions is novel and shows the potential of this technique, in particular, the use of ceramic gaskets that are more stable at higher temperatures and the lack of a hydrostatic compression medium. Thus, the technique is ideally suited to characterize the thermal-elastic properties of hard materials such as transition metal carbides.

ACKNOWLEDGMENTS

Part of this research was supported through the projects "GeoMaX" funded under the Emmy-Noether Program of the German Science Foundation (No. MA4534/3-1) as well as Grant No. MA4534/4-1. H.M. acknowledges support from the Bavarian Academy of Sciences. We acknowledge technical assistance from A. Ehnes and I. Schwark from the sample environment group at PETRA III within the framework of the Extreme Conditions Science Infrastructure ECSI). We thank J. Mainberger for preparing the carbide samples for the carbon analysis and Martin Harms for proofreading and reformatting the reference list.

REFERENCES

[1]M. J. Gasch, D. T. Ellerby, and S. M. Johnson, in *Handbook of Ceramic Composites*, edited by N. P. Bansal (Kluwer Academic Publishers, Boston, MA, 2005), pp. 197–224.
[2]K. Upadhya, J. M. Yang, and W. P. Hoffmann, Am. Ceram. Soc. Bull. **76**, 51 (1997).
[3]L. E. Toth, *Transition Metal Carbides and Nitrides* (Academic Press, New York, 1971).
[4]W. S. Williams, Mater. Sci. Eng. A **105-106**, 1 (1988).
[5]K. Hackett, S. Verhoef, R. A. Cutler, and D. K. Shetty, J. Am. Ceram. Soc. **92**, 2404 (2009).
[6]X.-X. Yu, C. R. Weinberger, and G. B. Thompson, Acta Mater. **80**, 341 (2014).
[7]B. D. Diwan, Can. J. Phys. **92**, 415 (2014).
[8]A. L. Bowman, J. Phys. Chem. **65**, 1596 (1961).
[9]A. I. Gusev, A. A. Rempel, and V. N. Lipatnikov, J. Phys. Condens. Matter **8**, 8277 (1996).
[10]K. Nakamura and M. Yashima, Mater. Sci. Eng. B **148**, 69 (2008).
[11]J. R. Cooper and R. L. Hansler, J. Chem. Phys. **39**, 248 (1963).
[12]G. Santoro and R. T. Dolloff, J. Appl. Phys. **39**, 2293 (1968).
[13]E. I. Isaev, S. I. Simak, I. A. Abrikosov, R. Ahuja, Y. K. Vekilov, M. I. Katsnelson, A. I. Lichtenstein, and B. Johansson, J. Appl. Phys. **101**, 123519 (2007).
[14]B. M. Klein, L. L. Boyer, and D. A. Papaconstantopoulos, Solid State Commun. **20**, 937 (1976).
[15]H. Li, L. Zhang, Q. Zeng, K. Guan, K. Li, H. Ren, S. Liu, and L. Cheng, Solid State Commun. **151**, 602 (2011).
[16]M. Sahnoun, C. Daul, M. Driz, J. C. Parlebas, and C. Demangeat, Comput. Mater. Sci. **33**, 175 (2005).
[17]H. G. Smith and W. Gläser, Phys. Rev. Lett. **25**, 1611 (1970).
[18]W. Weber, Phys. Rev. B **8**, 5082 (1973).
[19]C. P. Kempter, Phys. Status Solidi B **36**, K137 (1969).
[20]C. R. Houska, J. Am. Ceram. Soc. **47**, 310 (1964).
[21]K. K. Kelley, J. Am. Chem. Soc. **62**, 818 (1940).
[22]R. O. Elliott and C. P. Kempter, J. Phys. Chem. **62**, 630 (1958).
[23]C. K. Jun and P. T. B. Shaffer, J. Less Common Met. **24**, 323 (1971).
[24]K. Frisk and A. Fernández Guillermet, J. Alloys Compd. **238**, 167 (1996).

[25]A. Krajewski, L. D'Alessio, and G. De Maria, Cryst. Res. Technol. **33**, 341 (1998).
[26]C. Kral, W. Lengauer, D. Rafaja, and P. Ettmayer, J. Alloys Compd. **265**, 215 (1998).
[27]A. Friedrich, B. Winkler, E. A. Juarez-Arellano, and L. Bayarjargal, Materials **4**, 1648 (2011).
[28]H. L. Brown, P. E. Armstrong, and C. P. Kempter, J. Chem. Phys. **45**, 547 (1966).
[29]R. W. Bartlett and C. W. Smith, J. Appl. Phys. **38**, 5428 (1967).
[30]C. K. Jun and P. T. B. Shaffer, J. Less Common Met. **23**, 367 (1971).
[31]S. P. Dodd, M. Cankurtaran, and B. James, J. Mater. Sci. **38**, 1107 (2003).
[32]H. P. Liermann, A. K. Singh, B. Manoun, S. K. Saxena, and C. S. Zha, Int. J. Refract. Metals Hard Mater. **23**, 109 (2005).
[33]L. López-de-la-Torre, B. Winkler, J. Schreuer, K. Knorr, and M. Avalos-Borja, Solid State Commun. **134**, 245 (2005).
[34]Z. Wu, X.-J. Chen, V. V. Struzhkin, and R. E. Cohen, Phys. Rev. B **71**, 214103 (2005).
[35]X.-G. Lu, M. Selleby, and B. Sundman, Acta Mater. **55**, 1215 (2007).
[36]F. Peng, L. Han, H. Fu, and X. Cheng, Phys. Status Solidi B **246**, 1590 (2009).
[37]H.-H. Chen, Y. Bi, H.-K. Mao, J.-A. Xu, L. Liu, Q.-M. Jing, Z. Li, X.-R. Chen, and Q.-M. Wang, Int. J. Refract. Metals Hard Mater. **41**, 627 (2013).
[38]Y. Liu, Y. Jiang, R. Zhou, and J. Feng, J. Alloys Compd. **582**, 500 (2014).
[39]G. Sai Gautam and K. C. Hari Kumar, J. Alloys Compd. **587**, 380 (2014).
[40]H.-R. Wenk, S. Matthies, R. J. Hemley, H.-K. Mao, and J. Shu, Nature **405**, 1044 (2000).
[41]S. Merkel, A. K. McNamara, A. Kubo, S. Speziale, L. Miyagi, Y. Meng, T. S. Duffy, and H.-R. Wenk, Science **316**, 1729 (2007).
[42]H. Marquardt and L. Miyagi, Nat. Geosci. **8**, 311 (2015).
[43]T. S. Duffy, G. Shen, D. L. Heinz, J. Shu, Y. Ma, H.-K. Mao, R. J. Hemley, and A. K. Singh, Phys. Rev. B **60**, 15063 (1999).
[44]B. Kiefer, S. R. Shieh, T. S. Duffy, and T. Sekine, Phys. Rev. B **72**, 014102 (2005).
[45]H. Dong, D. He, T. S. Duffy, and Y. Zhao, Phys. Rev. B **79**, 014105 (2009).
[46]S. Merkel, H.-P. Liermann, L. Miyagi, and H.-R. Wenk, Acta Mater. **61**, 5144 (2013).
[47]H.-K. Mao, R. J. Hemley, and A. L. Mao, in *Advances in High Pressure Research in Condensed Matter: Proceedings of the International Conference on Condensed Matter Under High Pressures*, edited by B. K. Godwal (NISCOM, New Delhi, 1997), pp. 12–19.
[48]H.-K. Mao, J. Xu, and P. M. Bell, J. Geophys. Res. **91**, 4673 (1986).
[49]Y. Fei, A. Ricolleau, M. Frank, K. Mibe, G. Shen, and V. Prakapenka, Proc. Natl. Acad. Sci. U.S.A. **104**, 9182 (2007).
[50]A. P. Hammersley, S. O. Svensson, M. Hanfland, A. N. Fitch, and D. Hausermann, High Press. Res. **14**, 235 (1996).
[51]A. Le Bail, H. Duroy, and J. L. Fourquet, Mater. Res. Bull. **23**, 447 (1988).
[52]L. Lutterotti, S. Matthies, H.-R. Wenk, A. S. Schultz, and J. W. Richardson, J. Appl. Phys. **81**, 594 (1997).
[53]H.-P. Liermann, S. Merkel, L. Miyagi, H.-R. Wenk, G. Shen, H. Cynn, and W. J. Evans, Rev. Sci. Instrum. **80**, 104501 (2009).
[54]H.-P. Liermann, Z. Konôpková, W. Morgenroth, K. Glazyrin, J. Bednarčik, E. E. McBride, S. Petitgirard, J. T. Delitz, M. Wendt, Y. Bican, A. Ehnes, I. Schwark, A. Rothkirch, M. Tischer, J. Heuer, H. Schulte-Schrepping, T. Kracht, and H. Franz, J. Synchrotron Radiat. **22**, 908 (2015).
[55]H.-R. Wenk, L. Lutterotti, P. Kaercher, W. Kanitpanyacharoen, L. Miyagi, and R. Vasin, Powder Diffr. **29**, 220 (2014).
[56]C.-M. Sung, C. Goetze, and H.-K. Mao, Rev. Sci. Instrum. **48**, 1386 (1977).
[57]A. K. Singh and G. C. Kennedy, J. Appl. Phys. **45**, 4686 (1974).
[58]A. K. Singh, J. Appl. Phys. **73**, 4278 (1993).
[59]T. Uchida, N. Funamori, and T. Yagi, J. Appl. Phys. **80**, 739 (1996).
[60]S. Merkel, N. Miyajima, D. Antonangeli, G. Fiquet, and T. Yagi, J. Appl. Phys. **100**, 023510 (2006).
[61]S. Merkel, C. Tomé, and H.-R. Wenk, Phys. Rev. B **79**, 064110 (2009).
[62]F. Birch, Phys. Rev. **71**, 809 (1947).
[63]T. S. Duffy and Y. Wang, "Ultrahigh-pressure mineralogy physics and chemistry of the earth's deep interior," in *Reviews in Mineralogy*, edited by R. J. Hemley (Mineralogical Society of America, Washington, DC, 1998), Vol. 37, pp. 425–457.
[64]C. Zener, *Elasticity and Anelasticity in Metals* (University of Chicago Press, Chicago, 1948).
[65]V. G. Bukatov, V. I. Knyazev, O. S. Korostin, and V. M. Baranov, Izvestiya Akademii Nauk SSSR, Neorganicheskie Materialy **11**, 367 (1975).
[66]H. Marquardt, S. Speziale, K. Marquardt, H. J. Reichmann, Z. Konôpková, W. Morgenroth, and H.-P. Liermann, J. Appl. Phys. **110**, 113512 (2011).
[67]A. K. Singh, High Temp. High Press. **10**, 641 (1978).
[68]J. D. Bass, R. C. Liebermann, D. J. Weidner, and S. J. Finch, Phys. Earth Planet. Inter. **25**, 140 (1981).
[69]G. R. Gruzalski and D. M. Zehner, Phys. Rev. B **34**, 3841 (1986).
[70]J.-H. Jhi, S. G. Louie, M. L. Cohen, and J. Ihm, Phys. Rev. Lett. **86**, 3348 (2001).
[71]X.-X. Yu, G. B. Thompson, and C. R. Weinberger, J. Eur. Ceram. Soc. **35**, 95 (2015).